Thin Solid Films 518 (2010) 4273–4280

Contents lists available at ScienceDirect

Thin Solid Films

journal homepage: www.elsevier.com/locate/tsf

A study of the nanostructure and hardness of electron beam evaporated TiAlBN Coatings

M.A. Baker [a,*], M.A. Monclus [b], C. Rebholz [c], P.N. Gibson [d], A. Leyland [e], A. Matthews [e]

[a] The Surface Analysis Laboratory, Faculty of Engineering and Physical Sciences, University of Surrey, Guildford GU2 7XH, UK
[b] National Physical Laboratory, Hampton Road, Teddington, TW11 0LW, UK
[c] Department of Mechanical and Manufacturing Engineering, University of Cyprus, 1678 Nicosia, Cyprus
[d] Institute for Health and Consumer Protection, Joint Research Centre, I-21027 Ispra (VA), Italy
[e] Department of Engineering Materials, University of Sheffield, Sheffield S1 3JD, UK

ARTICLE INFO

Article history:
Received 21 July 2009
Received in revised form 22 December 2009
Accepted 22 December 2009
Available online 11 January 2010

Keywords:
Nanocomposites
Thin films
Hardness
TiAlBN
X-ray photoelectron spectroscopy
X-ray diffraction
Transmission electron microscopy

ABSTRACT

TiAlBN coatings have been deposited by electron beam (EB) evaporation from a single TiAlBN material source onto AISI 316 stainless steel substrates at a temperature of 450 °C and substrate bias of −100 V. The stoichiometry and nanostructure have been studied by X-ray photoelectron spectroscopy, X-ray diffraction and transmission electron microscopy. The hardness and elastic modulus were determined by nanoindentation. Five coatings have been deposited, three from hot-pressed TiAlBN material and two from hot isostatically pressed (HIPped) material. The coatings deposited from the hot-pressed material exhibited a nanocomposite nc-(Ti,Al)N/a-BN/a-(Ti,Al)B_2 structure, the relative phase fraction being consistent with that predicted by the equilibrium Ti–B–N phase diagram. Nanoindentation hardness values were in the range of 22 to 32 GPa. Using the HIPped material, coating (Ti,Al)$B_{0.29}N_{0.46}$ was found to have a phase composition of 72–79 mol.% nc-(Ti,Al)$(N,B)_{1-x}$+21–28 mol.% amorphous titanium boride and a hardness of 32 GPa. The second coating, (Ti,Al)$B_{0.66}N_{0.25}$, was X-ray amorphous with a nitride+boride multiphase composition and a hardness of 26 GPa. The nanostructure and structure–property relationships of all coatings are discussed in detail. Comparisons are made between the single-EB coatings deposited in this work and previously deposited twin-EB coatings. Twin-EB deposition gives rise to lower adatom mobilities, leading to (111) (Ti,Al)N preferential orientation, smaller grain sizes, less dense coatings and lower hardnesses.

1. Introduction

In recent years, there has been increasing interest in the deposition of nanocomposite coatings with improved mechanical properties through plasma-assisted physical vapour deposition (PVD) methods [1]. The generalised nanocomposite coating structure consists of one or more hard nanocrystalline phase, usually a transition metal nitride or carbide, and one (or more) amorphous phases. The amorphous composition (and phase fraction) is chosen such that it is immiscible with the hard phase and offers enhanced mechanical properties such as superhardness [2], high hardness/elastic modulus (H/E) ratio [3] or low friction [4,5]. One of the most important nanocomposite coatings systems investigated to date is the Ti–B–N system and Veprek has reviewed much of this work [6]. Superhard TiBN coatings with a hardness of 55 GPa are obtainable by sputtering, when the nanostructure consists of equal fractions of TiN and TiB_2 phases [7].

TiAlBN coatings have been found to form similar nanocomposite structures to TiBN coatings, the addition of Al resulting in its substitution for Ti in the nanocrystalline titanium nitride phase. TiAlBN coatings deposited by plasma-assisted twin electron beam (EB) evaporative PVD have shown excellent thermal stability, mechanical properties and field trial results for coated drills when comprised of a nc-(Ti,Al)N/a-BN nanocomposite coating structure [8,9]. Recent results have also shown TiAlBN coatings to exhibit oxidation resistance to temperatures above 800 °C [10].

Compared to twin-EB evaporation, the use of a single-EB source could simplify the deposition process and reduce costs. Hence, the aim of this paper is to determine the nanostructure and mechanical properties of five TiAlBN coatings deposited by single-EB evaporation (a single material source) using two different evaporative materials; a hot-pressed material and hot isostatically pressed (HIPped) material. The composition of the hot-pressed material was selected with the intention of depositing coatings with a nc-(Ti,Al)N/a-BN structure and the composition of the HIPped material was selected to deposit coatings with a nc-TiN/a-TiB_2 structure. The hardness and elastic modulus of the coatings were determined by nanoindentation and the nanostructure characterised using X-ray photoelectron spectroscopy (XPS), glancing angle X-ray diffraction (GAXRD) and transmission electron microscopy (TEM). These results allow a useful comparison to be made between the nanostructure and mechanical properties of

* Corresponding author.
E-mail address: m.baker@surrey.ac.uk (M.A. Baker).

0040-6090/$ – see front matter © 2010 Elsevier B.V. All rights reserved.
doi:10.1016/j.tsf.2009.12.109

single-EB compared to twin-EB TiAlBN coatings grown using essentially the same deposition equipment and experimental conditions.

2. Experimental details

TiAlBN coatings, 2.0 ± 0.2 μm thick, were deposited onto polished AISI 316 substrates ($R_a = 0.02$ μm) by evaporating different TiAlBN materials in Ar or in Ar/N_2 gas mixtures, using a TECVAC IP70L industrial-scale triode ion plating unit with a base pressure of $<5 \times 10^{-4}$ Pa. The deposition pressure, substrate temperature, bias voltage were kept constant at 0.5 Pa, 450 °C, −100 V respectively. Under these deposition conditions, it is estimated that the average ion deposition energy is approximately 30–40 eV. Prior to deposition the AISI 316 stainless steel substrates were ultrasonically cleaned in acetone and isopropanol and then fixed in a single-rotation holder mounted 300 mm above the vapour source. A commercially available hot-pressed TiAlBN material, used widely to manufacture resistive evaporation boats (consisting of 50 wt.% TiB_2, 30 wt.% BN and 20 wt.% AlN [11]), and, for this study, a specially developed HIPped TiAlBN material (consisting of 60 wt.% Ti, 30 wt.% TiB_2 and 10 wt.% AlN), were crushed and placed as granules into a crucible and EB evaporated for film deposition. The evaporation material mixtures used are given in Table 1.

Both the chemical and phase composition of the various coatings were determined by XPS, using a VG-Scientific Sigma Probe spectrometer employing a monochromated Al-Kα source and a hemispherical analyser. A pass energy/step of 20/0.1 eV was used for narrow scans. The spectrometer was calibrated using the Au $4f_{7/2}$ and Cu $2p_{3/2}$ peaks, with adventitious hydrocarbon contamination assigned to a C 1s peak binding energy of 285.0 eV. Prior to analysis, samples were etched using a 3 keV argon ion beam, until the oxygen 1s peak reached a stable minimum value. Quantification of the data involved Shirley background subtraction and the use of instrument-modified Wagner sensitivity factors. The crystallographic structure and texture of the films were analysed by GAXRD, using CuK_α radiation at an incident angle of 1°. The X-ray generator settings were 35 kV and 30 mA, the step angle being 0.2°. TEM studies were performed using a Philips CM200 microscope operated at 200 keV and employing a LaB_6 filament. Specimen preparation involved grinding and polishing down the stainless steel substrate, followed by dimpling and ion beam thinning.

The mechanical properties of TiAlBN coatings were determined by nanoindentation using a CSM Nanohardness Tester. Indentations were made with a Berkovich diamond tip using an average of 10 loading–unloading cycles (maximum load of 5 mN; loading/unloading rates of 10 mN/min) for the estimation of elastic modulus and hardness. The maximum indentation depth was less than 10% of the film thickness, thus avoiding significant substrate contribution to the measured data values. The indenter tip shape was calibrated against a fused silica counterface, according to standard procedures [12].

Table 1
Chemical composition and stoichiometry of the TiAlBN coatings.

Sample	Evaporation material	Coating colour	Coating elemental concentration [at.%]				Stoichiometry
			Ti	Al	B	N	
1	'New' Ti–Al–B–N source material	Metallic black	15.3	6.4	39.6	38.7	$(Ti,Al)B_{1.82}N_{1.78}$
2	'Old' Ti–Al–B–N source material[a]	Purple	12.1	7.0	33.4	47.5	$(Ti,Al)B_{1.75}N_{2.49}$
3	50% 'new'+50% 'old' Ti–Al–B–N material+N_2 (10 ml/min)	Purple	21.6	5.1	24.5	48.8	$(Ti,Al)B_{0.92}N_{1.83}$
H1	HIPped Ti–Al–B–N material	Metallic grey	47.9	4.4	34.5	13.2	$(Ti,Al)B_{0.66}N_{0.25}$
H2	HIPped Ti–Al–B–N material+N_2 (20 ml/min)	Metallic grey	52.4	4.6	16.8	26.2	$(Ti,Al)B_{0.29}N_{0.46}$

[a] Previously used material.

3. Results

3.1. XPS — Chemical and phase composition, phase fraction and bonding

The chemical composition of the samples was determined from the Ti 2p, Al 2p, B 1s and N 1s XPS peak areas. The compositions of the coatings are given in Table 1. The concentration of Al in both the hot-pressed and HIPped targets is approximately 8 at.%. The Al concentrations found in the deposited coatings were 5–7 at.% for the HIPped coatings and 4–5 at.% for the hot-pressed coatings. For the TiAlBN coatings, the stoichiometries are given in the form $(Ti,Al)B_xN_y$ as the presence of low concentrations of Al (compared to Ti) is known to result in Al substitution into the TiN and TiB_2 phases to form (Ti,Al)N and $(Ti,Al)B_2$ respectively [8,9,13].

In Fig. 1, the compositions of all the coatings have been superimposed onto the Ti–B–N phase diagram of Novotny [14]. As expected, the three coatings deposited from the HIPped material $(Ti,Al)B_{1.82}N_{1.78}$, $(Ti,Al)B_{1.75}N_{2.49}$ and $(Ti,Al)B_{0.92}N_{1.83}$ have compositions which lie close to the (Ti,Al)N–BN tie line. However, the two samples deposited from the hot-pressed material, $(Ti,Al)B_{0.29}N_{0.46}$ and $(Ti,Al)B_{0.66}N_{0.25}$, lie on the $(Ti,Al)B–(Ti,Al)N_{1-x}$ rather than the anticipated $(Ti,Al)B_2$–(Ti,Al)N tie line.

XPS spectra from TiB_2, TiN and h-BN standard materials have previously yielded B 1s peak positions of 187.8 eV and 190.5 eV for TiB_2 and BN, and N 1s peak positions of 397.2 eV and 398.1 eV for TiN and BN respectively [15]. Peak fitted XPS B 1s and N 1s spectra for the TiAlBN coatings deposited from the hot-pressed material are shown in Fig. 2. The peaks can be fitted into their (Ti,Al)N, BN and $(Ti,Al)B_2$ components (the binding energies of all components being within 0.2 eV of the previously obtained values [15]). A small third component at higher binding energies was also used in the B 1s and N 1s fits, corresponding to sub-oxide species of B and N (associated with the high reactivity of Ti, Al and B with oxygen and the formation of a sub-monolayer of oxide, even under ultra high vacuum conditions). Earlier work has shown that for samples in the TiN+BN+TiB_2 three phase region, phase fractions calculated directly from the coating stoichiometry can be compared to those determined from the B 1s and N 1s peak fits [15]. The phase fraction results for coatings $(Ti,Al)B_{1.82}N_{1.78}$, $(Ti,Al)B_{1.75}N_{2.49}$ and $(Ti,Al)B_{0.92}N_{1.83}$ are given in Table 2. These agree well with those predicted by the phase diagram, as found for earlier TiBN and TiAlBN coatings with such three phase compositions [15,16].

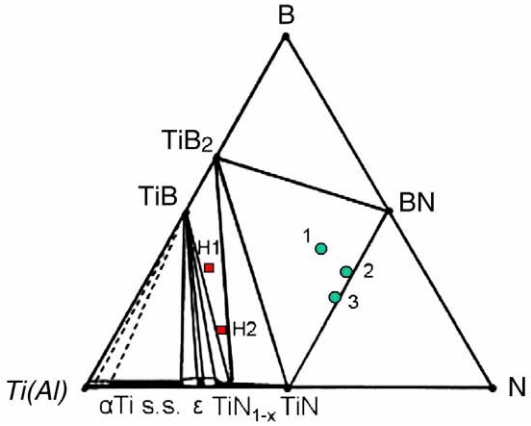

Fig. 1. A Ti–B–N equilibrium phase diagram of Novotny [14] modified for TiAlBN PVD deposited coatings. Superimposed on the diagram are the coating compositions deposited using the hot-pressed material (1, 2 and 3) and HIPped material (H1 and H2).

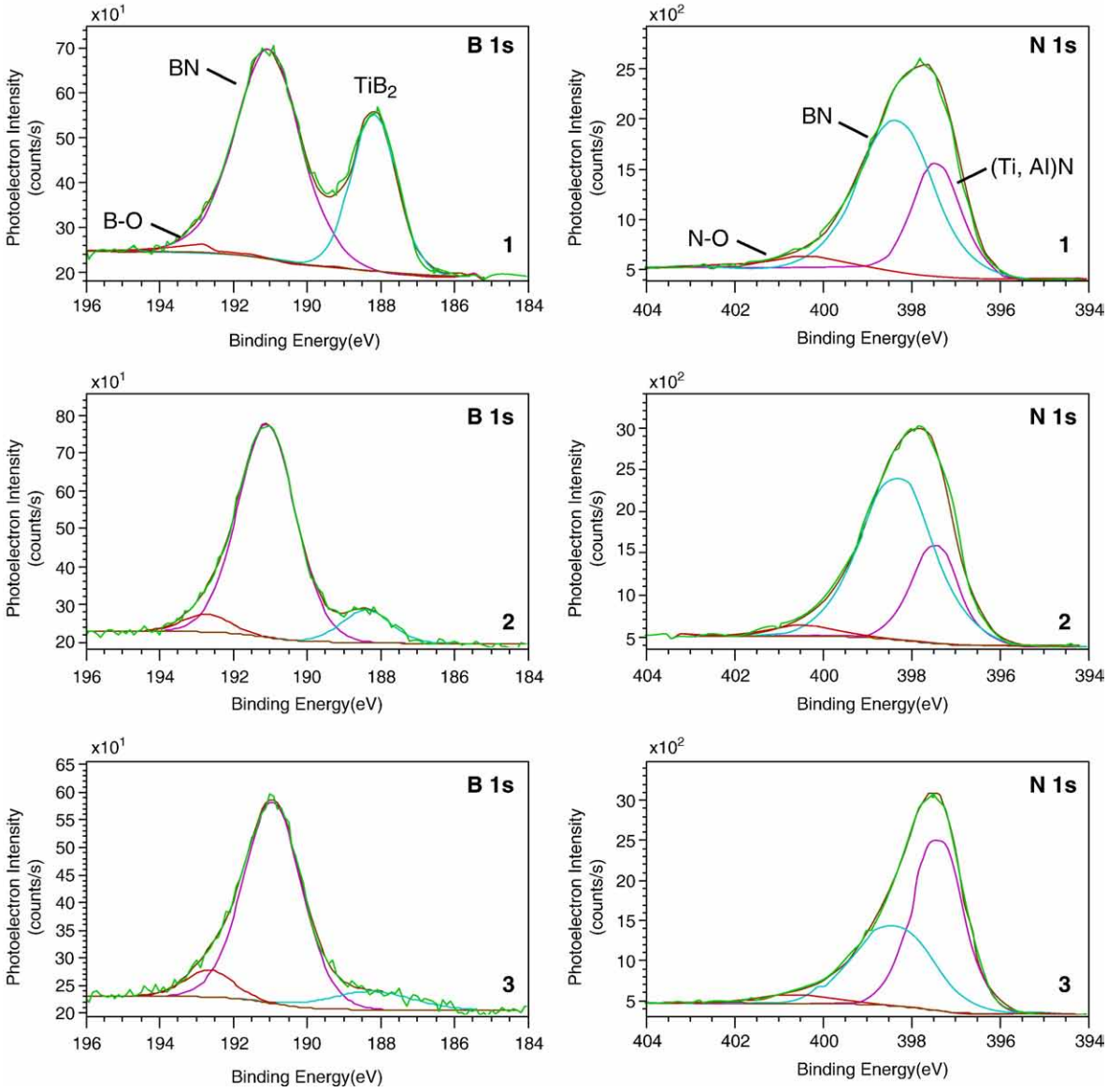

Fig. 2. Peak fitted XPS spectra a) B 1s and b) N 1s for TiAlBN coatings 1, 2 and 3 deposited from the hot-pressed material.

B 1s and N 1s XPS spectra of the coating deposited from the HIPped material, $TiB_{0.66}N_{0.25}$ and $TiB_{0.29}N_{0.46}$ are shown in Fig. 3. Coating $TiB_{0.66}N_{0.25}$ exhibits a single B 1s component at 187.5 eV. Coating $TiB_{0.29}N_{0.46}$ also exhibits this component at 187.5 eV, and in addition a second component at 186.0 eV. Recently, we have undertaken XPS analysis of an aerospace material (Ti–6Al–4 V+8.1 vol.% TiB) and the presence of TiB as the only boride phase was confirmed by XRD. XPS analysis showed the B 1s peak position for TiB to have a binding energy of 187.7 eV, only 0.1 eV shifted from the B 1s binding energy for TiB_2. These similar binding energies result from the strong B–B bonding dominating over Ti–B bonding found for both TiB and TiB_2 [17,18]. Due to the similarity in the B 1s binding energies for TiB and TiB_2, the boride phase composition for this coating cannot be unequivocally determined from these XPS results. The B 1s component at 186.0 eV has been previously observed in other work on TiAlBN coatings by the authors and has been ascribed to B incorporation into (Ti,Al)N nanocrystallites [16]. The N 1s peak for both $TiB_{0.66}N_{0.25}$ and $TiB_{0.29}N_{0.46}$ is comprised of a single main component at 397.2 eV. This peak position is consistent with that of (Ti,Al)N.

Table 2
Relative phase fractions for the TiAlBN coatings deposited from the hot-pressed material. The 'Calc' values have been calculated directly from the stoichiometry and the 'Exp' values determined by curve fitting the XPS N 1s and B 1s peaks (methods described in detail in [15]).

Coating	Stoichiometry	(Ti,Al)N		BN		$(Ti,Al)B_2$	
		Calc.	Exp.	Calc.	Exp.	Calc.	Exp.
1	$(Ti,Al)B_{1.82}N_{1.78}$	31	31	53	55	16	14
2	$(Ti,Al)B_{1.75}N_{2.49}$	36	39	61	58	3	3
3	$(Ti,Al)B_{0.92}N_{1.83}$	52	51	46	47	2	2

3.2. XRD — crystallographic phase determination, grain size and structural evaluation

The XRD data for the two sets of coatings are shown in Fig. 4. The results for the three phase coatings deposited from the hot-pressed material ($(Ti,Al)B_{1.82}N_{1.78}$, $(Ti,Al)B_{1.75}N_{2.49}$ and $(Ti,Al)B_{0.92}N_{1.83}$), show there to be a single Ti-containing nanocrystalline phase present, f.c.c. (Ti,Al)N. The XRD pattern for coating H2, deposited from the HIPped target also shows diffraction peaks corresponding to (Ti,Al)N.

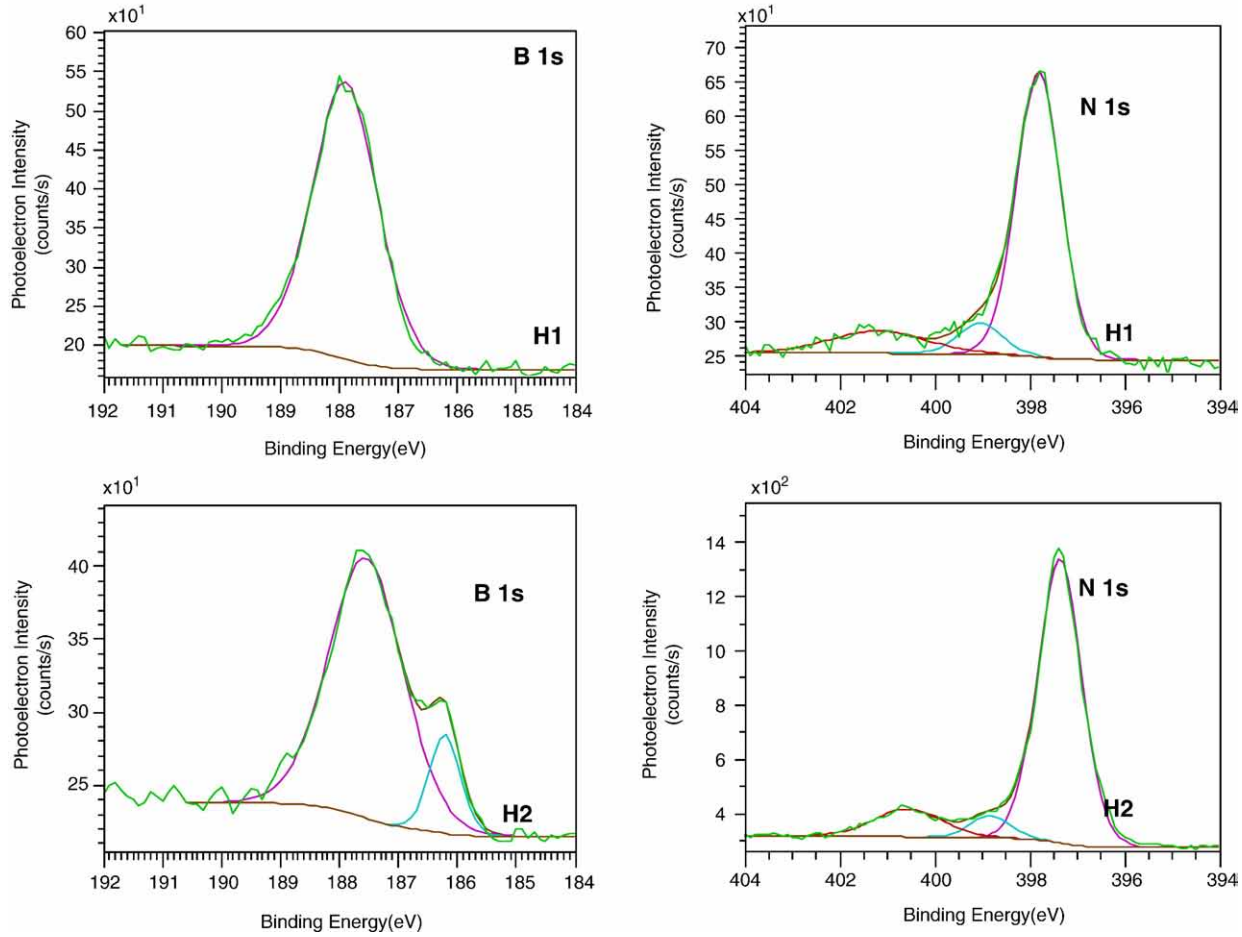

Fig. 3. Curve fitted XPS B 1s and N 1s spectra for TiAlBN coatings H1 and H2, deposited from the HIPped material.

All of these 4 coatings exhibit a weak (200) preferential orientation. The BN, $(Ti,Al)B_2$ and (Ti,Al)B phases present in these TiAlBN coatings are probably amorphous (as found in other TiBN and TiAlBN coatings with similar phase compositions) [8,15], and/or are at a concentration too low for XRD detection, although there is a slight indication of a second nanocrystalline structure in coating 1, probably $(Ti,Al)B_2$.

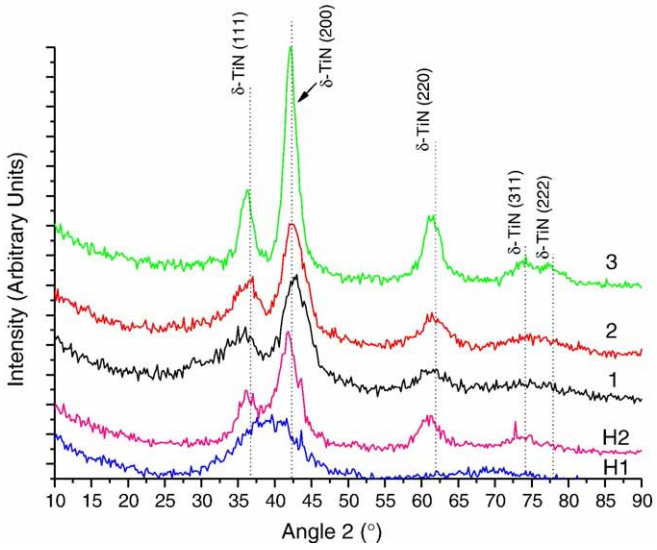

Fig. 4. XRD spectra of TiAlBN coatings deposited with a hot-pressed target (coatings 1–3) and a HIPped target (H1 and H2).

From the Ti(Al)BN phase diagram in Fig. 1, a sub-stoichiometric (Ti,Al) N_{1-x} phase might be expected in coating H2. However, the XRD peak position shift to lower angles for this coating corresponds to an increase in lattice parameter, rather than the smaller lattice parameter expected for a sub-stoichiometric phase. The increase in the lattice parameter can be explained by the incorporation of B into the TiN lattice, resulting in the formation of a Ti(N,B) phase. Mayrhofer et al. have shown this to be the case both theoretically and experimentally [19]. Taking into account the broad features at 40° and 70° in the diffraction pattern of sample H1, the disappearance of the (220) peak, and also the SAD pattern of Fig. 6, it can be concluded that the structure of sample H1 is essentially amorphous.

Grain size estimates were made adopting a single line method based on least-squares fitting to a pseudo-Voigt function [20]. The method was applied to the TiN (200) peak, for which it was assumed that Gaussian broadening is due to strain and Lorentzian broadening is due to crystallite size. Grain size estimates for coatings 1, 2, 3 and H2 are ~1.3, 2.0, 5.2, and 1.8 nm respectively.

Fig. 5 shows TEM dark field plan view images and SAD patterns for coatings 1, 2 and 3. SAD patterns for coatings 2 and 3 exhibit rings that can be indexed to the (111), (200), (220) and (311) orientations of the (Ti,Al)N cubic phase. The SAD pattern for coating 1 exhibits fewer and dimmer rings, but the (Ti,Al)N (200), (220) and (311) rings can be distinguished.

Average measurements taken from a number of crystallites evident in the dark field images for coatings 1, 2 and 3 gave average grain sizes of approximately 1, 3 and 5 nm respectively, in excellent agreement with the XRD results. This reduction in grain size is due to competitive grain growth as the concentrations of the BN, $(Ti,Al)B_2$ and/or (Ti,Al)B phases increase.

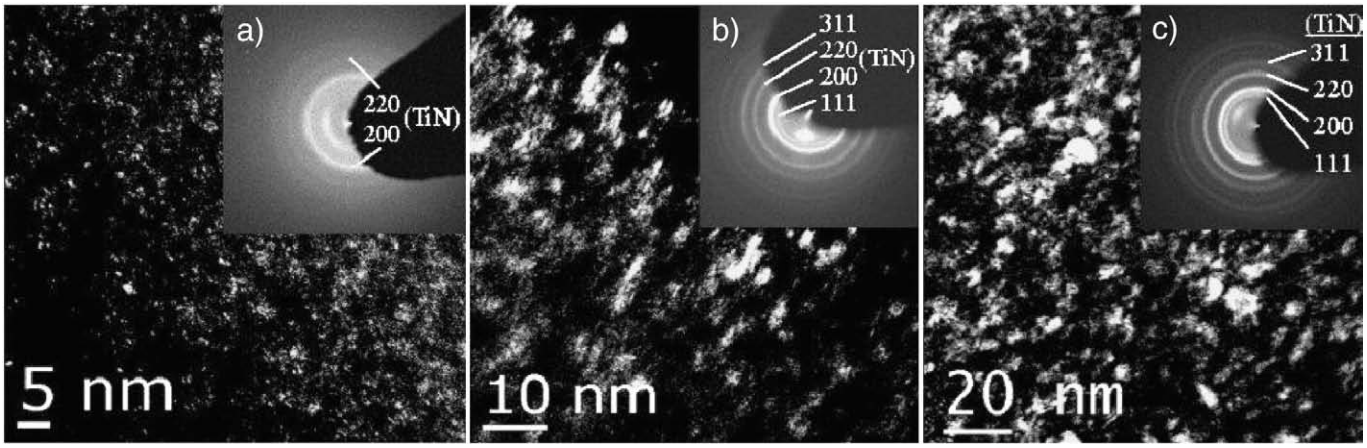

Fig. 5. TEM dark field images and selected area diffraction patterns for TiAlBN coatings 1 (a), 2 (b) and 3 (c).

Fig. 6 presents similar TEM data for coatings H1 and H2 plus a high resolution (HR) image for H2. Sample H1 exhibits a SAD pattern characteristic of an amorphous material (Fig. 6a), while sample H2 displays a ring pattern characteristic of a nanocrystalline material with reflections assigned to the (Ti,Al)N cubic phase, with average grain sizes of ~2–3 nm (Fig. 6b). Numerous lattice fringes can be observed in the HR image for H2 coating (Fig. 6c), and a number of individual nanocrystals can be resolved. An inverse Fourier-Transform image highlighting (200) and (111) oriented (Ti,Al)N nanocrystals is shown in Fig. 6c inset.

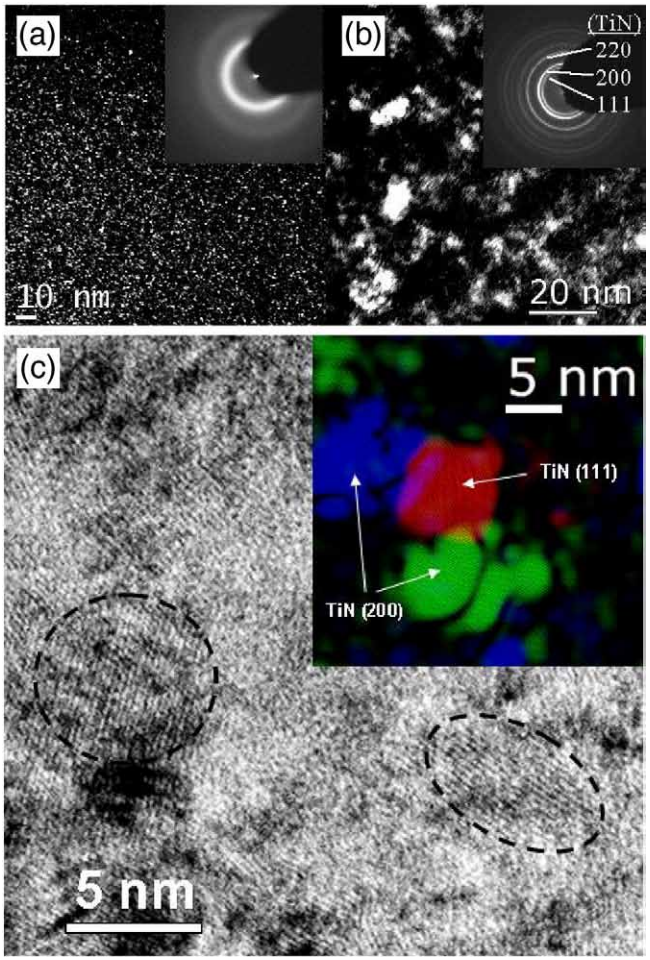

Fig. 6. TEM dark field images and selected area diffraction patterns and for TiAlBN coatings H1 (a) and H2 (b), and a high resolution image for coating H2 (c), with an inverse Fourier Transformed filtered image as an inset, highlighting the (Ti,Al)N nanocrystals.

3.3. Mechanical properties — nanoindentation

Hardness and elastic modulus results for the TiAlBN coatings are presented in Fig. 7. The highest hardness of 32 GPa observed both for coatings 3 and H2 is clearly associated with their higher (Ti,Al)N content. Lower hardness values are found for the amorphous coating, H1, and for coatings 1 and 2 due to the higher BN phase fraction and very small grain size (leading to an inverse Hall–Petch effect). The H/E ratios for coatings 3 and H2 are both 0.11, i.e. approximately double the values for single phase transition metal nitride coatings, such as TiN and CrN.

4. Discussion

In this paper, the coating nanostructure and mechanical properties have been presented for various TiAlBN coatings deposited from a single-EB vapour source. It is interesting to compare these results to those previously presented for TiAlBN coatings deposited from a twin-EB system (concurrent Ti and TiAlBN evaporation material) employing essentially the same deposition equipment [8,9]. For both the single- and twin-EB deposition runs, a substrate temperature of 450 °C and substrate bias voltage of −100 V were employed. The deposition pressures were 0.5 Pa for the single-EB coatings and

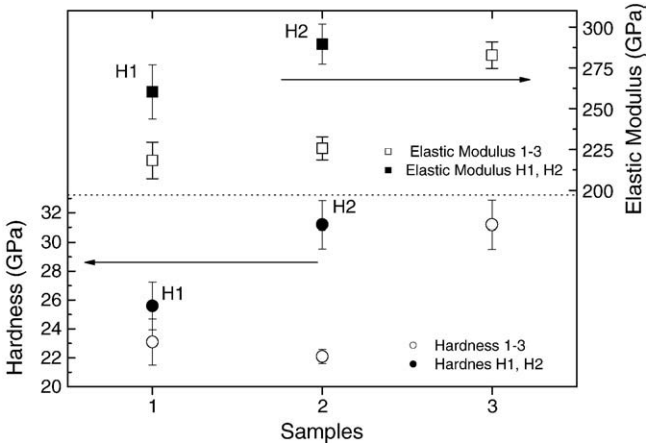

Fig. 7. Hardness values for TiAlBN coatings. Open symbols (○, □) correspond to coatings 1, 2 and 3 and filled symbols (●, ■) correspond to H1 and H2.

0.35 Pa for the twin-EB coatings. A comparison of the chemical composition, phase fraction, nanostructure and mechanical properties of coatings 2 and 3 (produced by single-EB deposition) with similar coating compositions deposited by twin-EB deposition is given in Table 3. (It should be noted that the phase compositions given for the coatings are an average of those calculated from the stoichiometry and those determined from curve fitting the XPS B and N 1s peaks.) XRD data, taken in the θ–2θ mode, for the twin-EB coatings [8,9] is presented in Fig. 8. All of these coatings (except for the highest B containing coating) exhibit a strong (111) preferential orientation. The single-EB coatings, however, show a weak (Ti,Al)N (200) preferential orientation (Fig. 4). In addition, the (Ti,Al)N (111) peaks for the twin-EB coatings in Fig. 8 are narrower than the (200) peaks, indicating that the nanocrystallites have a needle-like morphology. For similar compositions and phase fractions of the single and twin-EB deposited coatings, the (Ti,Al)N grain size and hardness are relatively higher for both of the single-EB coatings.

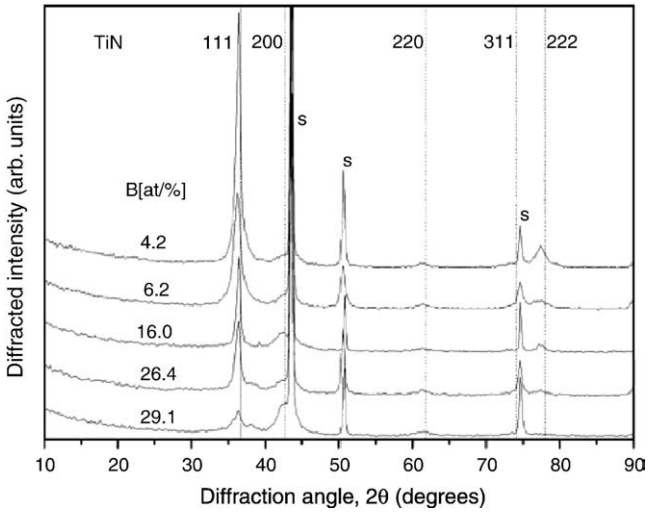

Fig. 8. XRD θ–2θ scans for the twin-EB deposited TiAlBN coatings. s = substrate peak (full details of the deposition conditions and properties are given in [9]).

4.1. Nanostructural evolution during film growth for the TiAlBN (nc-(Ti,Al)N/a-BN) coatings deposited using hot-pressed evaporant material

Petrov et al. have discussed in detail the influence of coating growth temperature, incident ion energy and ion flux on the TiN preferential growth direction and shown that by varying the deposition parameters the growth mechanism can be switched between (111) and (200) preferential orientations [21]. Preferential orientation occurs due to a lower surface adatom diffusivity on a particular crystallographic plane (e.g. (111)) giving rise to faster growth of nanocrystallites with that orientation [21]. Petrov et al. state that the rate-limiting step for transition metal nitride film growth is cation incorporation and that TiN coatings grown at high N_2^+/Me flux ratios exhibit a (200) preferential orientation and lower N_2^+/Me flux ratios give rise to a (111) preferential orientation [21]. Thus, at high N_2^+/Me flux ratios, adatoms remain longer on the (200) surface than the (111) surface. Patsalas et al. have grown TiN coatings by sputtering, employing very similar deposition conditions to those used for our EB coatings (substrate temperature of 400 °C and a bias voltage −100 V) and found that such deposition parameters lead to (200) preferentially oriented coatings [22]. The results of Petrov et al. [21] and Patsalas et al. [22] indicate that deposition conditions which generally promote higher adatom mobilities (high temperature, substrate bias and ion flux) lead to (200) preferentially oriented TiN coatings. As a (111) preferential orientation is associated with a lower surface mobility, it might be expected that for coatings with a very similar phase composition, the twin-EB deposited (111) oriented TiAlBN coatings would show smaller grain sizes than the weak (200) preferential orientated single-EB coatings, as is observed for coatings 3 and 60 in Table 3.

Considering now the origin of the different (Ti,Al)N preferential orientations for the single-EB deposited coatings compared to the twin-EB deposited coatings, the substrate temperature and negative bias voltage were the same, hence the (111) preferential orientation for the twin-EB deposited coatings arises either from a lower N_2^+/Me flux or a higher deposition rate for this process giving rise to an lower overall adatom mobility [21].

The single- and twin-EB deposited coatings employed very similar deposition systems, the IP70L and IP35L respectively. The IP70L has a slightly larger chamber volume ($W \times D \times H$) of $700 \times 700 \times 700$ mm, compared to $500 \times 500 \times 700$ mm for the IP35L system. The IP35L system has a smaller source to substrate distance and the use of HIPped material in this system rather than the hot-pressed material in the single-EB IP70L system enabled higher EB powers to be employed for the twin-EB deposition. Both of these factors result in higher deposition rates for the twin-EB deposited coatings. Consequently, the lower adatom mobility, giving rise to the (111) preferential orientation for the twin-EB deposited coatings appears to arise primarily from the higher deposition rates achieved in the IP35L system.

4.2. Nanostructure-hardness correlation for the TiAlBN (nc-(Ti,Al)N/a-BN) coatings deposited using hot-pressed evaporant material

With regard to the measured hardness of these nanocomposite coatings, for similar compositions the single-EB coatings exhibit higher values than the twin-EB coatings. It has been argued that for many nanocomposite coating systems the highest hardness will be observed when the nanocrystallites are covered in a monolayer of the amorphous phase [e.g. 2,5]. However, for the single- and twin-EB coatings shown in Table 3, the grain sizes and amorphous phase fraction is such that for all coatings, the nanocrystallites will have an amorphous phase coverage of greater than one monolayer [23]. In our previous work on twin-EB TiAlBN coatings, the highest hardness was found for nc-(Ti,Al)N/a-BN coatings with a 5 nm grain size [9]. This is consistent with the highest hardness being found for the single-EB coating 3 in Table 3.

Table 3
A comparison of elemental and phase composition, (Ti,Al)N grain size, preferential orientation, hardness and elastic modulus for similar single-EB and twin-EB deposited TiAlBN coatings (twin-EB coating data taken from [8,9]).

Coating	Elemental composition				Phrase fraction			Grain size (nm)	(Ti,Al)N preferential orientation	Hardness (GPa)	Elastic modulus (GPa)
	Ti	Al	B	N	(Ti,Al)N	BN	(Ti,Al)B_2				
2 (single)	12	7	33	48	38	59	3	2.0	Very weak (200)	22	225
40 (twin)	10	11	29	49	44	55	1	≈1	Random	21	240
3 (single)	22	5	25	49	52	47	2	5.2	Very weak (200)	32	277
60 (twin)	17	9	26	48	52	45	3	3.0	(111)	23	260

There are however, several other factors which may affect hardness, such as phase separation, density and preferential orientation. With regard to phase separation, our previous results showed that twin-EB deposited coatings with high BN phase fractions (2 and 3) exhibited no change in hardness upon annealing to 900 °C [9]. Hence, as the single-EB coatings apparently exhibit higher adatom mobilities than the twin-EB deposited coatings, it can be considered that both the single and twin-EB TiAlBN coatings are fully phase separated and this parameter is not affecting the hardness of the coatings. Studies of single crystal and nanostructured TiN coatings show no significant difference in the hardness between (200) and (111) preferentially oriented TiN coatings [24,25]. Hence, crystallite orientation does not appear to directly influence hardness. However, in this work, the twin-EB deposited nc-(Ti,Al)N/a-BN coatings, with a (111) preferential orientation, show a lower hardness than the single-EB deposited nc-(Ti,Al)N/a-BN coatings. From the results of Petrov et al. [21] and Patsalas et al. [22], lower adatom mobilities lead to the (111) preferential orientation. Table 3 appears to support the hypothesis that lower adatom mobilities for the twin-EB (111) preferentially oriented coatings should also give rise to very small grain sizes. In addition, the nanocrystallites in twin-EB coatings have a needle-like morphology. From our previous work on the twin-EB coatings, the coating density was measured and it was found that as the needle-like morphology became more pronounced, the density decreased [9].

Interestingly, Yang et al. have reported that for TiN/CrN superlattice coatings, a (111) orientation gives rise to a lower hardness than a (200) preferential orientation and attributed this to less effective interface–dislocation interactions for the (111) oriented superlattice coatings, leading to more dislocations propagating across these interfaces [26]. Interface–dislocation interactions will also be important to the hardness of nanocomposite systems such as these nc-(Ti,Al)N/a-BN coatings and as found for the TiN/CrN superlattices, a (111) preferred orientation my give rise to a lower hardness.

To summarise, the observed lower hardness for the two twin-EB deposited coatings is probably associated with a lower adatom mobility promoting (Ti,Al)N (111) preferential growth, which gives rise to very small grain sizes, needle-like nanocrystallite morphologies, a less dense structure and also possibly weaker interface–dislocation interactions.

4.3. Nanostructure of the TiAlBN coatings deposited using the HIPped material

When plotted on the Ti(Al)BN phase diagram (Fig. 1), the composition of the two single-EB coatings deposited from the HIPped material places them in a region where their equilibrium phase composition is dependent on the composition of the sub-stoichiometric (Ti,Al)N_{1-x} phase. The possible phase compositions are Ti(Al,B)+Ti(Al)N_{1-x}, (Ti,Al)B_2+(Ti,Al)N_{1-x} or Ti(Al,B)+(Ti,Al)B_2+(TiAl)N_{1-x}. For coating H2, the XRD results clearly indicate the formation of a (Ti,Al)N nanocrystalline phase. From the XPS spectra it is not clear if the boride phase is (Ti,Al)B or (Ti,Al)B_2. Previously, it has been found that for TiBN coatings lying along the TiN–TiB_2 tie line, the phase composition is in good agreement with that predicted by the phase diagram [27], and it has been shown in this paper that the single-EB coatings 1–3 deposited from the hot-pressed material also show good agreement with the phase diagram. Consequently, it is not unreasonable to expect that the phase composition of these HIPped material coatings, H1 and H2, will also be in general agreement with the phase diagram. The X-ray amorphous nature of coating H1 results from the high content of amorphous boride phase(s) and if the coating has a three rather than a two phase composition then also from strong competitive phase growth.

It is interesting to examine the phase composition for coating H2, (Ti,Al)$B_{0.29}N_{0.46}$, in more detail and compare the GAXRD and XPS results recorded here with those of Mayrhofer et al. [19] for a PACVD $TiB_{0.40}N_{0.83}$ coating grown at a substrate temperature of 510 °C and substrate bias of −500 V. The $TiB_{0.40}N_{0.83}$ coating of Mayrhofer et al., lies very close to the TiB_2–TiN tie line and both coatings have the same B concentrations (16.7 at.% [19] and 16.8 at.% [Table 1]), hence might be expected to contain similar boride phase contents.

In coating H2, the XPS B 1s peak shows two components, the peak at 187.5 eV is ascribed to (Ti,Al)B or (Ti,Al)B_2 and the peak at 186.0 eV corresponds to B substituting into the (Ti,Al)N_{1-x} phase to give (Ti,Al)$(N,B)_{1-x}$ [16]. Consequently, there is good agreement between our results and those of Mayrhofer et al. with regard to B substitution into the nitride phase. The peak area ratio of the B 1s 187.5/186.0 eV peaks in Fig. 3 is 6.2, hence it can be calculated that approximately 2.7 at.% B is being incorporated into the (Ti,Al)$(N,B)_{1-x}$ phase. As 14.1 at.% of B is bonded as boride and 26.2 at.%N+2.7 at.% B is bonded in the nitride phase, the phase fractions for the extreme situations of the phase composition being (Ti,Al)B+(Ti,Al)$(N,B)_{1-x}$ or (Ti,Al)B_2+(Ti,Al)$(N,B)_{1-x}$ can be calculated. These phase fractions for H2 would be 28 mol.% (Ti,Al)B+72 mol.% (Ti,Al)$(N,B)_{0.67}$ or 21 mol.% (Ti,Al)B_2+79 mol.% (Ti,Al)$(N,B)_{0.58}$ respectively. Consequently, for all of the possible two or three phase compositions of coating H2, there would be at least a 21 mol.% boride phase fraction.

In contrast, based purely upon XRD measurements, Mayrhofer et al. have proposed that no boride phase is present in their $TiB_{0.40}N_{0.83}$ coating, instead a significant fraction of 16.7 at.% B is incorporated into a single Ti(N,B) phase with the remainder being associated with 'B-rich domains' located at grain boundaries [19]. Their experimental XRD data gave a lattice parameter value of 0.4315 nm for the Ti(N,B) phase, compared to a lattice parameter of 0.4240 nm for stoichiometric f.c.c. TiN. Similar to the results of Mayrhofer et al., coating H2 also shows an XRD peak shift to lower angles corresponding to an increase in the lattice parameter for the (Ti,Al)$(N,B)_{1-x}$ phase. In this (Ti,Al)$(N,B)_{1-x}$ nanocrystalline phase, Al has substituted into f.c.c. TiN to form (Ti,Al)N and the nitride phase is sub-stoichiometric. Interestingly, both of these deviations from pure stoichiometric TiN might be expected to cause a slight decrease in the lattice parameter [28,29]. However, as the lattice parameter is observed to increase and not decrease, it is the incorporation of B into the nitride phase which is having the largest effect on the lattice parameter. From the XRD spectrum, the lattice parameter for the (Ti,Al)$(N,B)_{1-x}$ phase of coating H2 is calculated to be 0.4325 nm. This value is similar to that obtained by Mayrhofer et al.

No XPS was undertaken in the work of Mayrhofer et al., so the presence of an amorphous phase could not be identified. The authors propose the formation of 'B-rich domains' at the grain boundary, but the composition and nature of these domains is unclear. From the results of this work, it seems most probable that the $TiB_{0.40}N_{0.83}$ coating deposited by Mayrhofer et al. had a two phase nc-Ti(N,B)/a-TiB_2 nanocomposite structure similar to the nc-(Ti,Al)$(N,B)_{1-x}$/a-(Ti,Al)B/(Ti,Al)B_2 structure observed for coating H2. Such a nanocomposite structure would also explain the high hardness of 42 GPa observed for their $TiB_{0.40}N_{0.83}$ coating [19].

With regard to the X-ray amorphous coating H1, from the XPS results, the coating clearly has a multiphase nitride+boride composition. The exact nature of these phases and the relative phase fractions again cannot be established, but there is definitely a higher fraction of boride than nitride. On the assumption that the phase composition is in agreement with the phase diagram and that this corresponds to the simplest two phase (Ti,Al)B+(Ti,Al)N_{1-x} structure, then the phase fraction (determined from the XPS chemical composition) would be 69 mol.% (Ti,Al)B+31 mol.% (Ti,Al)$N_{0.74}$. The nanostructure of this coating is clearly at the boundary between a fully amorphous structure, and what might be termed an "ultra-nanocrystalline" structure, with dimensions in the sub-nanometer range.

4.4. Nanostructure-hardness correlation for the TiAlBN coatings deposited using the HIPped material

The nanocomposite coating H2 shows a hardness of 32 GPa and the amorphous coating H1 a hardness of 26 GPa. Coating H2 has a (Ti,Al)

$(N,B)_{1-x}$ phase content of between 72 and 79 mol.% and a very weak preferential (200) orientation. Furthermore, this coating has a nc-(Ti,Al)$(N,B)_{1-x}$ grain size of 1.8 nm and an a-TiB/TiB_2 phase fraction of 21–28 mol.%. This combination of grain size and amorphous phase fraction gives rise to approximate a-TiB/TiB_2 monolayer coverage of the (Ti,Al)$(N,B)_{1-x}$ grains [23], ideal to attain high hardness [2]. Thus, the relatively high hardness of coating H2 arises from its high (Ti,Al)$(N,B)_{1-x}$ phase fraction with monolayer coverage of grains. A higher hardness may have been achieved by increasing the grain size (to approximately 5 nm) and a more complete phase segregation (no B incorporation in the (Ti,Al)N phase) through modifying the deposition conditions or by age hardening [9,19].

Coating H1 shows a rather high hardness considering its apparent amorphous structure. However, the XPS results indicate the presence of separate boride and nitride phases in this coating. All of the possible phases (in their crystalline form) are hard materials ($H \geq 20$ GPa) and multiphase nanostructured coatings generally show higher hardnesses than their single phase counterparts. In addition, these boride and nitride phases, although X-ray amorphous, are probably "ultra-nanocrystalline" with an exceptionally small grain size (<1 nm). Consequently, the multiphase structure of hard compounds and possible presence of hardening nanocrystalline phase(s) can explain the relatively high hardness (26 GPa) observed for this coating.

5. Conclusions

The nanostructure and hardness of single-EB-evaporated TiAlBN coatings deposited using hot isostatically pressed (HIPped) and hot-pressed TiAlBN material at a substrate temperature of 450 °C and substrate bias of −100 V have been reported. The Al concentration was kept low at 4–7 at.%.

(1) The three coatings deposited with the hot-pressed evaporant material exhibited a three phase nanostructure of nc-(Ti,Al)N+a-BN+a-(Ti,Al)B_2. The phase composition and relative phase fraction was in good agreement with that expected from the Ti–B–N equilibrium phase diagram. Two of these coatings (Ti,Al)$B_{0.92}N_{1.83}$, and (Ti,Al)$B_{1.75}N_{2.49}$ contained a low (Ti,Al)B_2 phase content and exhibited grain sizes of 5.2 and 2.0 nm with hardnesses of 32 and 22 GPa respectively. The limited hardness values are associated with high a-BN contents of 47 and 58 mol.% respectively. When compared to twin-EB TiAlBN coatings with very similar phase compositions deposited previously, the single-EB coatings exhibited higher hardness values. The lower hardness of the twin-EB coatings has been attributed to a lower adatom mobility, giving rise to (Ti,Al)N (111) preferential growth, very small grain sizes, a lower density and also possibly weaker interface–dislocation interactions.

(2) Two TiAlBN coatings were deposited with the HIPped material. Coating (Ti,Al)$B_{0.29}N_{0.46}$ was found to have a phase composition of 72–79 mol.% nc-(Ti,Al)$(N,B)_{1-x}$+21–28 mol.% amorphous titanium boride. 2.7 at.% B was incorporated into the (Ti,Al)$(N,B)_{1-x}$ phase and the (Ti,Al)$(N,B)_{1-x}$ stoichiometry was between (Ti,Al)$(N,B)_{0.58}$ and (Ti,Al)$(N,B)_{0.67}$. Although the exact nature (and hence relative phase fractions) of the titanium boride phase(s), TiB and TiB_2, could not be determined, the coating structure and phase composition appears to be in good agreement with the equilibrium phase diagram. The relatively high hardness of this coating (32 GPa) is attributed to a nc-(Ti,Al)$(N,B)_{1-x}$ grain size of 1.8 nm and an amorphous boride phase fraction of 21–28 mol.%, giving rise to approximate titanium boride monolayer coverage of the (Ti,Al)$(N,B)_{1-x}$ grains. The second coating deposited from the hot-pressed target ((Ti,Al)$B_{0.66}N_{0.25}$), was X-ray amorphous with a multiphase nitride+boride phase composition (higher fraction of boride than nitride). Its hardness of 26 GPa is attributed to it having an extremely fine multiphase nanostructured composition of hard boride and nitride compounds.

(3) A useful comparison has been made of the microstructure and hardness of TiAlBN deposited on similar single and twin-EB beam equipment. The higher deposition rate employed on the twin-EB beam rig led to lower adatom mobilities on the coating surface during growth, giving rise to a (Ti,Al)N (111) preferential orientation and coatings with a lower hardness.

References

[1] P.H. Mayrhofer, C. Mitterer, L. Hultman, H. Clemens, Prog. Mater. Sci. 51 (2006) 1032.
[2] S. Veprek, J. Vac. Sci. Technol. A 17 (1999) 2401.
[3] M.A. Baker, P.J. Kench, C. Tsotsos, A. Leyland, A. Matthews, J. Vac. Sci. Technol. A 23 (2005) 423.
[4] R. Goller, P. Torri, M.A. Baker, R. Gilmore, W. Gissler, Surf. Coat. Technol. 120–121 (1999) 453.
[5] K. Polychronopoulou, J. Niedhardt, C. Rebholz, M.A. Baker, M. O'Sullivan, A.E. Reiter, A.E. Gunnaes, K. Giannakopoulos, C. Mitterer, J. Mater. Res. 23 (2008) 3048.
[6] S. Veprek, M.G.J. Veprek-Heijman, P. Karvankova, J. Prochazka, Thin Solid Films 476 (2005) 1.
[7] P. Hammer, A. Steiner, R. Villa, M.A. Baker, P.N. Gibson, J. Haupt, W. Gissler, Surf. Coat. Technol. 68/69 (1994) 194.
[8] M.A. Baker, S. Klose, C. Rebholz, A. Leyland, A. Matthews, Surf. Coat. Technol. 151–152 (2002) 338.
[9] C. Rebholz, M.A. Monclus, M.A. Baker, P.H. Mayrhofer, P.N. Gibson, A. Leyland, A. Matthews, Surf. Coat. Technol. 201 (2007) 6078.
[10] M. Pfeiler, J. Zechner, M. Penoy, C. Michotte, C. Mitterer, M. Kathrein, Surf. Coat. Technol. 203 (2009) 3104.
[11] U. Goetz, Innovation in ceramics, Sintec-Group, Halblech, Germany, 2005. www.sintec-keramik.com/sintec-en/evaporator-boats_properties.html.
[12] W.C. Oliver, G.M. Pharr, J. Mater. Res. 7 (1992) 1564.
[13] M.A. Monclus, M.A. Baker, V. Stolojan, C. Rebholz, P.N. Gibson, A. Leyland, A. Matthews, Surf. Inter. Anal. 38 (2006) 731–735.
[14] H. Novotny, F. Benesovsky, C. Brukl, O.M. Schod, Chemistry 92 (1961) 403–414.
[15] M.A. Baker, T.P. Mollart, P.N. Gibson, W. Gissler, J. Vac. Sci. Technol. A 15 (1997) 284.
[16] M.A. Baker, C. Rebholz, A. Leyland, A. Matthews, Vacuum 67 (2002) 471.
[17] K.B. Panda, K.S.R. Chandran, Comp. Mater. Sci. 35 (2006) 134.
[18] K.B. Panda, K.S.R. Chandran, Acta Mater. 54 (2006) 1641.
[19] P.H. Mayrhofer, M. Stoiber, C. Mitterer, Scr. Mater. 53 (2005) 241.
[20] T.H. de Keijser, E.J. Mittemeijer, H.C. Rozendaal, J. Appl. Cryst. 16 (1983) 309.
[21] I. Petrov, P.B. Barna, L. Hultman, J.E. Greene, J. Vac. Sci. Technol. A 21 (2003) S117.
[22] P. Patsalas, C. Charitidis, S. Logothetidis, Surf. Coat. Technol. 125 (2000) 335.
[23] M.A. Baker, Surf. Coat. Technol. 201 (2007) 6105.
[24] H. Ljungcrantz, M. Oden, L. Hultman, J.E. Greene, J.E. Sundgren, J. Appl. Phys. 80 (1996) 6725.
[25] C.-H. Ma, J.-H. Huang, H. Chen, Surf. Coat. Technol. 200 (2006) 3868.
[26] Q. Yang, C. He, L.R. Zhao, J.-P. Immarigeon, Scr. Mater. 46 (2002) 293.
[27] T.P. Mollart, M.A. Baker, J. Haupt, A. Steiner, P. Hammer, W. Gissler, Surf. Coat. Technol. 74/75 (1995) 491.
[28] D. McIntyre, J.E. Greene, G. Håkansson, J.-E. Sundgren, W.-D. Munz, J. Appl. Phys. 67 (1990) 1542.
[29] L.-J. Meng, M.P. dos Santos, Surf. Coat. Technol. 90 (1997) 64.